PAPER

New opportunities for tailored nanoparticle catalysts through exsolution from inherently disordered defect fluorite-type oxides†

William S. J. Skinner, [ID] *[a] Eleonora Calì,[b] Angelos K. Bonis,[c] Gwilherm Kerherve,[a] Kalliopi Kousi [ID] [c] and David J. Payne*[ad]

Nanoparticle exsolution from oxide supports has emerged as a promising strategy for designing highly active and stable catalysts, with perovskite oxides being the most explored support structures to date. In this study, we successfully demonstrate exsolution from the novel $Y_2Zr_{2-x}Ru_xO_7$ ($0 \leq x \leq 0.2$) defect fluorite system, probe the factors governing the extent of exsolution in this system, and evaluate the performance of these exsolved materials as catalysts for CO_2 conversion. X-ray photoelectron spectroscopy measurements performed both under vacuum and near-ambient pressure conditions give unique insight into the evolution of the chemical state of ruthenium substituents during exsolution, providing evidence for the existence of intermediate reduction steps before eventual reduction to metallic ruthenium. The distribution of chemical states and extent of reduction to metallic ruthenium exhibit a strong dependence on both the duration and temperature of the reductive treatment applied, with both potentially limiting the extent of reduction at a given partial pressure of oxygen. STEM-EDX characterisation reveals the formation of well-dispersed metallic ruthenium nanoparticles over the unique, nanoporous morphology of the host structure. Preliminary testing for the reverse-water-gas-shift reaction demonstrates promising performance, achieving CO_2 conversion close to thermodynamic equilibrium and 100% CO selectivity above 650 °C. These findings provide new insights into exsolution from the defect fluorite system and expand the range of host materials available within the exsolution design space for advanced catalysts in energy-related applications.

Introduction

Heterogeneous catalysts play a key role in the industrial production of critical fuels and chemicals, including hydrogen,[1] liquid hydrocarbon fuels[2] and ammonia.[3] Interest has grown in recent years towards leveraging heterogeneous catalysts for carbon capture and conversion,[4] simultaneously reducing emissions and utilising captured CO_2 through conversion to fuels or value-added chemicals, the production of which might otherwise rely on crude oil.[5] As is the case for the majority of industrial catalysts, CO_2 conversion catalysts are typically composed of nanoparticles of an active component dispersed on a high surface area solid. Such a catalyst structure produces a high surface-area-to-volume ratio, maximising the number of active sites available to participate in catalytic reactions and ensuring effective utilisation of the active component.[6] For catalytic CO_2 conversion, nanoparticles are typically metals chosen for their activity and selectivity toward specific target products, while the solid host is often a refractory metal oxide (*e.g.*, TiO_2, ZrO_2, Al_2O_3) that is cost-effective, exhibits high specific surface area and demonstrates high thermal and chemical stability.[7] Other favourable support properties, all of which play an important role in determining catalyst activity, include a high capacity for storage and release of oxygen, acid–base characteristics, and participation in electron transfer processes.[8,9] The properties of a heterogeneous catalyst are therefore not defined solely by the active component, but also by its support, the nature of the interface between them, and their metal–support interactions.[10] Careful consideration should thus be given towards the choice of active metal, oxide support and the nature of the interface between them, which will depend on the method of preparation.

A number of methods are commonly employed to disperse active metal nanoparticles over the surface of a host oxide, with the choice of method playing an important role in determining the metal–metal oxide interface and governing the morphology,

aDepartment of Materials, Imperial College London, Exhibition Road, London SW7 2AZ, UK. E-mail: william.skinner17@imperial.ac.uk; d.payne@imperial.ac.uk

bDepartment of Applied Science and Technology (DISAT), Politecnico di Torino, 10129 Torino, Italy

cSchool of Chemistry and Chemical Engineering, University of Surrey, GU2 7XH, UK

dNEOM Education, Research, and Innovation Foundation, Al Khuraybah, Tabuk 49643-9136, Saudi Arabia

This journal is © The Royal Society of Chemistry 2025

J. Mater. Chem. A, 2025, 13, 6451–6468 | 6451

size, dispersion and stability of the active component.[7] As such, the development of new methods of active catalyst dispersal that enable fine-tuning of these properties – while remaining cost-effective and industrially scalable – is an active research area across the field of heterogeneous catalysis, particularly in the case of CO_2 conversion catalysts, which must be designed to withstand deactivation mechanisms including sintering, poisoning and carbon deposition.[11]

One method that has shown great promise is to grow metallic nanoparticles directly from an oxide support in which host cations have been substituted to some degree by cations of the active component.[12] This process in which substituent species are driven from the bulk to form metallic nanoparticles, leaving the host structure intact, is referred to as nanoparticle exsolution, and can be triggered through a variety of different treatments,[13] but consistently produces fine, well-distributed metallic nanoparticles that are anchored – or 'socketed' – in

the material, endowing them with excellent stability against deactivation.[14,15]

To date, nanoparticle exsolution studies have predominantly centred around ABO_3 perovskite oxide systems, owing to their structural stability, compositional flexibility and ability to accommodate a wide range of dopants.[16–18] The exsolution mechanism in this system comprises a complex series of processes, with diffusion and reduction steps preceding the nucleation and growth of nanoparticles.[19] Our understanding of nanoparticle nucleation and growth from the ABO_3 perovskite system has been driven forward considerably by *in situ* TEM[20] and HAADF-STEM[21] imaging of the early stages of exsolution; however, the preceding reduction and migration steps are more challenging to probe experimentally, and as a result have been based primarily on computational modelling. One model proposes that migration of substituent B-site cations to the surface of the perovskite becomes thermodynamically
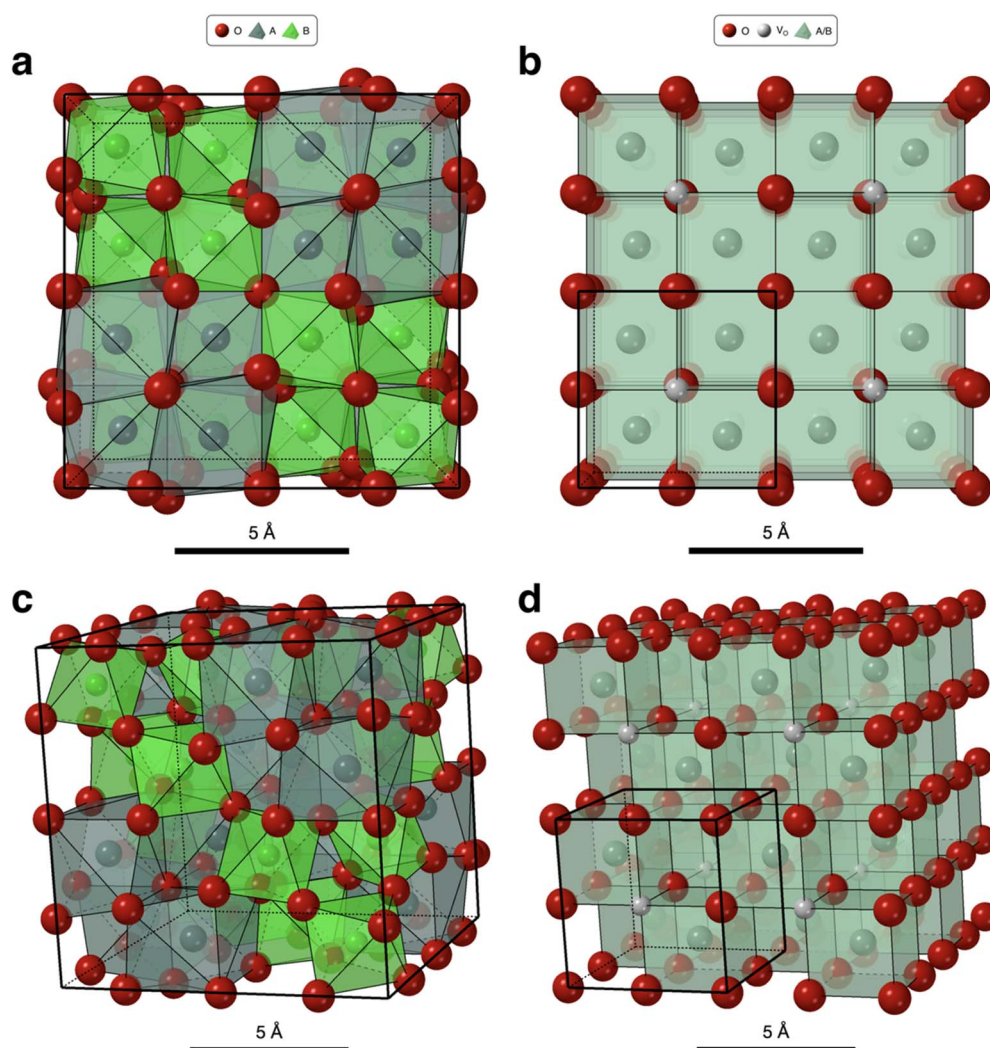

Fig. 1 (a) and (c) Crystal structure of the ideal cubic pyrochlore $A_2B_2O_7$ (space group $Fd\bar{3}m$). In a III–V pyrochlore oxide, A^{3+} and B^{4+} occupy the 16d and 16c sites, respectively. O^{2-} occupies two inequivalent positions: the 8b and 48f sites. (b) and (d) A simplified schematic of the defect fluorite $A_2B_2O_7$ crystal structure (space group $Fm\bar{3}m$). In a III–V defect fluorite oxide, A^{3+} and B^{4+} both occupy the 4a site in a statistically disordered manner. O^{2-} occupies the 8c site, with 1 in 8 sites vacant to maintain the $A_2B_2O_7$ stoichiometry. Visualisation was performed with the CrystalMaker software.

6452 | *J. Mater. Chem. A*, 2025, **13**, 6451–6468

This journal is © The Royal Society of Chemistry 2025

favourable under reducing conditions, and precedes reduction to neutral species.[22] A contrasting model recently proposed by Bonkowski *et al.* suggests that reduction of substituent B-site cations to neutral species occurs within the perovskite lattice, followed by migration to form either bulk or surface nanoparticles, driven by neutral species being energetically unfavoured in the perovskite lattice.[23] These models are invaluable in providing the foundation from which to design systematic experimental investigations of exsolution from a range of systems under different conditions, in order to build upon our understanding of this complex phenomenon and develop robust process and material design principles for exsolution.

An important next step in developing our understanding of nanoparticle exsolution and expanding the application of exsolved materials is the exploration of exsolution from other, non-perovskite oxides.[24] $A_2B_2O_7$ pyrochlore- and defect fluorite-type oxides (Fig. 1) are particularly interesting as alternative host structures for exsolution, as they exhibit high thermal stability and oxygen ion mobility,[25] the capacity for mixed ionic-electronic conduction,[26] and compositional flexibility.[27] $A_2B_2O_7$ oxides can also accommodate larger A-site cations than perovskites owing to their more open structure, alongside a variety of B-site cations that are less stable or uncommon in perovskites, providing the opportunity to explore new stoichiometries that are not available in the ABO_3 perovskites.[28] Defective fluorite-type structures present a particularly interesting alternative host structure for exsolution, as they exhibit very high intrinsic concentration of oxygen vacancies,[29] which are well established to play a key role in nanoparticle exsolution.[16] To date, the application of $A_2B_2O_7$ pyrochlore- and defect fluorite-type oxides as hosts for nanoparticle exsolution has been very limited, but promising, warranting further investigation.[30]

In this study, we aim to expand the understanding of exsolution in non-perovskite systems by systematically probing the exsolution of ruthenium from the $Y_2Zr_{2-x}Ru_xO_7$ system, which exhibits a defective fluorite-type structure, under a range of different reducing environments. We then evaluate the performance of exsolved $Y_2Zr_{1.8}Ru_{0.2}O_7$ towards CO_2 conversion *via* the reverse-water-gas-shift reaction, a key method of converting captured CO_2 into value-added products. By gaining insights into the complex manner in which the chemical state of ruthenium evolves throughout the exsolution process, and better understanding the factors that govern the extent of exsolution in this system, this study seeks to develop our understanding of the exsolution mechanism in $A_2B_2O_7$ systems, guiding the design of future $A_2B_2O_7$-based catalyst materials and facilitating comparative analysis between exsolution from these systems and the widely studied ABO_3 perovskites. It is our hope that this work will highlight the potential of these systems as a new family of hosts for exsolved materials, stimulating further work in this area.

Experimental

Synthesis and catalyst preparation

$Y_2Zr_{2-x}Ru_xO_7$ (*x* = 0, 0.1, 0.2) was synthesized by a citrate sol–gel method. The raw materials used throughout this method include yttrium(III) oxide (99.999% trace metals basis, Sigma-Aldrich), ruthenium nitrosyl nitrate solution (1.5% w/v (Ru), Thermo Scientific Acros), zirconyl nitrate solution (≥99% trace metals basis, Sigma-Aldrich), citric acid monohydrate (Fisher Chemical), ethylene glycol (EMSURE Supelco, Sigma-Aldrich) nitric acid (68% w/w, Primar Plus, Fisher Chemical) and ammonia (25% w/v, EMSURE Supelco, Sigma-Aldrich).

Firstly, an yttrium(III) nitrate precursor solution was prepared by weighing the appropriate mass of yttrium(III) oxide (following drying at 400 °C for 4 hours) and dissolving in an excess of 3.0 M nitric acid (molar ratio $HNO_3 : Y_2O_3 = 10 : 1$), stirring under reflux at 80 °C until full dissolution had occurred. After cooling to room temperature, stoichiometric amounts of the zirconyl nitrate and ruthenium nitrosyl nitrate precursors were added, and the solution was stirred for one hour. Ethylene glycol and 1.0 M citric acid were then added such that the ratio of total metal cations to ethylene glycol to citric acid was 1 : 4 : 4, after which the pH was adjusted to 7 by dropwise addition of 2.0 M NH_4OH under continuous monitoring with a pH meter. In the absence of a detailed understanding of ion speciation in this system, a pH of 7 was chosen to maximise the formation of citrate complexes, enhancing the homogeneity of the resulting gel, while remaining at sufficiently low pH values so as to avoid precursor hydrolysis.[31,32] After stirring and heating under reflux at 80 °C for 3 hours to ensure a homogeneous distribution of precursors, the solution was slowly evaporated by heating at 80 °C for 24 hours, until a viscous gel was formed. Combustion of this gel was performed by heating at 400 °C for 6 hours. Due to the highly exothermic nature of this combustion reaction, a ramp rate of 0.5 °C min^{-1} was used. The resulting powder was then calcined at 1000C for 1 hour, with a ramp rate of 5 °C min^{-1}, to obtain a pure phase of $Y_2Zr_{2-x}Ru_xO_7$.

The prepared $Y_2Zr_{2-x}Ru_xO_7$ (*x* = 0.0, 0.1, 0.2) samples were each reduced with a 6-hour isothermal hold at 1000 °C under flowing 5% H_2/N_2. A ramp rate of 5 °C min^{-1} under flowing 5% H_2/N_2 was used. For simplicity, as a range of reduction temperatures were employed in this study, reduced samples are referred to as $Y_2Zr_{2-x}Ru_xO_7$-R*XX*, where *XX* refers to the hundreds of degrees at which reduction took place (*e.g.*, R04 for a sample reduced at 400 °C, R10 for a sample reduced at 1000 °C). All other reduction conditions (an atmosphere of flowing 5% H_2/N_2, a ramp rate of 5 °C min^{-1} and an isothermal hold duration of 6 hours) are held constant.

X-ray diffraction

Powder X-ray diffraction (PXRD) patterns were collected using a Malvern PANalytical X'Pert Pro MPD diffractometer, operating at 40 kV and 40 mA with Cu Kα radiation ($\lambda = 1.5418$ Å). Phase identification was performed using the Malvern Panalytical HighScore Plus software[33] and the ICDD PDF-4+ database.[34] Peak indexing was performed in GSAS-II,[35] with corresponding lattice parameters calculated in UnitCell. Sample preparation consisted of carefully spreading a uniform layer of finely ground powder into a zero-background silicon sample holder. Details of all data processing performed on PXRD data between

This journal is © The Royal Society of Chemistry 2025

J. Mater. Chem. A, 2025, **13**, 6451–6468 | **6453**

acquisition and plotting are provided in the Methods section of the ESI.†

X-ray photoelectron spectroscopy

X-ray Photoelectron Spectroscopy (XPS) spectra were recorded using a Thermo Scientific K-Alpha spectrometer. The system operates at a base pressure of 8×10^{-9} mbar. The K-Alpha is equipped with a monochromated, micro-focused Al Kα X-ray source ($h\nu = 1486.6$ eV) and a 180° double focusing hemispherical analyser, with a 128-channel detector. The X-ray source was operated at an anode bias of 12 kV and an emission current of 6 mA. The maximum spot size was 400 μm². The energy scale of the analyser was calibrated using the Ag $3d_{5/2}$ peak (368.2 eV) of a sputter-cleaned silver internal reference. Sample charging during measurement was minimised with an in-built dual-beam source, consisting of an ultra-low energy co-axial electron and Ar⁺ ion beam. Samples were mounted onto a tantalum sample plate by pressing a uniform layer of finely ground powder onto a square of conductive copper tape. Core level and survey spectra were recorded with pass energies of 20 eV and 200 eV, respectively. Peak fitting and relative atomic percentage calculations (using the TPP-2M-corrected areas of the relevant peaks and their respective sensitivity factors) were performed using the Thermo Avantage software. Details on the peak models employed in this study and all data processing performed on XPS data between acquisition and plotting are provided in the Methods section of the ESI.†

Near-ambient pressure X-ray photoelectron spectroscopy

Lab-based near-ambient pressure X-ray photoelectron spectroscopy (NAP-XPS)[36–39] measurements were conducted on a HiPP-Lab system at Imperial College London. The system incorporates a monochromated Al Kα X-ray source ($h\nu = 1486.6$ eV), a concentric hemispherical analyser with differential pumping stages (HiPP-3, Scienta Omicron) and a 2D detector, consisting of a CCD camera coupled with a multi-channel plate. The energy scale of the analyser was calibrated using the Ag $3d_{5/2}$ peak (368.2 eV) of a sputter-cleaned silver reference foil (99.999% purity, Sigma-Aldrich), mounted alongside the pelletised sample on a stainless steel Omicron sample plate. During measurements, the sample was housed in a reaction chamber that comprises an X-ray transparent window, gas dosing lines, and a cone (0.8 mm diameter) which fits onto the entrance lens of the analyser. The partial pressures of O₂, Ar and H₂ in the analysis chamber were maintained at 0.5 mbar by varying the gas flow rates using mass flow controllers. All gases were purified with gas purifiers (MicroTorr, Saes) before flowing into the analysis chamber.[36] Sample heating was performed with a resistive heater, which automatically varies the power based on the sample temperature measured with a thermocouple in direct contact with the sample plate. Peak fitting was performed using the CasaXPS software package. Details on the NAP-XPS measurement protocol, the peak models employed in this study and all data processing performed on NAP-XPS data

between acquisition and plotting are provided in the Methods section of the ESI.†

Electron microscopy

SEM analysis was performed using a Thermo Fisher Apreo 2 SEM operated in secondary electron imaging mode at an accelerating voltage of 1 kV. Samples were imaged before and after reduction and after catalytic testing, and prepared by mounting the powders to SEM stubs with carbon tape. Imaging was conducted under high vacuum at working distances of 3–5 mm and a magnification range of 10 000–100 000.

TEM and STEM-EDX analysis were performed using a JEOL JEM-2100F TEM (operated at 200 kV, equipped with a CMOS 11 Mpx camera and Gatan EDX detector) and a Thermo Scientific Talos F200X TEM (operated at 200 kV, equipped with a CMOS 16 Mpx camera and Gatan EDX detector). Samples were imaged and analysed before and after reduction at various temperatures, and after catalytic testing, and were prepared by drop-casting powder previously dispersed and sonicated in analytical grade propan-2-ol (10 μL) on holey-C coated Cu grids (TAAB, 3.05 mm, 300 mesh). Particle size analysis was performed using Fiji.[40] Details on the methodology for particle size analysis are provided in the Methods section of the ESI.†

Catalytic testing

The reverse water gas shift (rWGS) reaction was carried out in a tubular fixed bed quartz reactor (30 cm length, 1 cm internal diameter). 0.2 g of catalyst was placed on quartz wool and the reactants were fed from the top of the reactor. The composition of these gases was recorded through a gas analyser and their total volumetric flow was measured with a bubble meter, which also measured the volumetric difference with the outlet gases. To analyse the product gases, an ABB AO2020 advanced optima process gas analyser was connected to the system that detected the volumetric flowrates of CO₂, CO, CH₄ and H₂. A K-type thermocouple was positioned directly above the catalyst bed to monitor the temperature throughout the experiment.
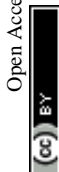
To remove any possible passivation layer, the exsolved sample (R10) was treated at 400 °C for 30 min under a 50 mL min⁻¹ flow of 10% H₂/N₂. The temperature was then increased to 500 °C for the catalytic test and measurements were recorded after stabilisation (approximately 30 min) at increments of 50 °C up to 800 °C and using a flow rate of 40 mL min⁻¹ of a 1 : 1 : 2 gas mixture of CO₂ : H₂ : N₂. The reverse-water-gas-shift reaction, alongside the equations utilised to measure the catalytic performance, are shown below:

$$CO_2 + 2H_2 \rightleftharpoons CO + 2H_2O \quad (1)$$
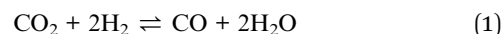
$$CO_2 \text{ conversion } (\%) = \frac{[CO_2]_{in} - [CO_2]_{out}}{[CO_2]_{in}} \times 100 \quad (2)$$

$$CO \text{ selectivity } (\%) = \frac{[CO]_{out}}{[CO_2]_{in} - [CO_2]_{out}} \times 100 \quad (3)$$

$$CH_4 \text{ selectivity } (\%) = \frac{[CH_4]_{out}}{[CO_2]_{in} - [CO_2]_{out}} \times 100 \quad (4)$$

6454 | J. Mater. Chem. A, 2025, 13, 6451–6468

This journal is © The Royal Society of Chemistry 2025

$[CO_2]_{in}$ is the initial CO_2 concentration in the gas mixture, and $[CO_2]_{out}$, $[CO]_{out}$ and $[CH_4]_{out}$ are the outlet concentrations of CO_2, CO and CH_4, respectively.

Thermodynamic simulations

ChemCad 7 software was employed to obtain thermodynamic equilibrium conversions for the reactants of the reverse-water-gas-shift reaction over a range of temperatures. The Soave Redlich Kwong (SRK) equation of state was used, and the reactor was simulated as a Gibbs reactor to calculate its thermodynamic equilibrium limits. The conditions of the experiment were replicated in the simulation, including the total inlet flowrate, reactant percentages and temperature of the reactor.

Surface area and porosity analysis

Surface area and porosity were characterised using a Micromeritics TriStar II 3020 surface area and porosity analyser. Nitrogen adsorption–desorption isotherms were measured at 77 K (-196 °C) in the relative pressure (P/P_0) range 0.08–0.31. Specific surface area was calculated using the Brunauer–Emmett–Teller (BET) method and pore size distribution was determined using the Barrett–Joyner–Halenda (BJH) method.

Results and discussion

Preparation and characterisation of $Y_2Zr_{2-x}Ru_xO_7$

The materials explored in this study, $Y_2Zr_{2-x}Ru_xO_7$ ($x = 0.0, 0.1, 0.2$), were prepared by a modified sol–gel method (detailed in the Synthesis and catalyst preparation sub-section of the Experimental section). PXRD patterns of these materials (Fig. 2a) demonstrate a close match to cubic $Y_2Zr_2O_7$ (space group $Fm\bar{3}m$) in PDF 01-081-8080,[34] with no residual unassigned peaks. $Y_2Zr_{2-x}Ru_xO_7$ ($x = 0.0, 0.1, 0.2$) thus share the same space group as the archetypal fluorite CeO_2, but with some notable differences. In the ideal fluorite CeO_2 structure, Ce^{4+} occupies the 4a site, eightfold coordinated by 8 O^{2-} ions, which occupy the 8c site. In the defective fluorite $Y_2Zr_2O_7$ structure, Y^{3+} and Zr^{4+} both occupy the 4a site, sevenfold coordinated by O^{2-} ions occupying the 8c site (1 in 8 sites are left vacant to maintain the $A_2B_2O_7$ stoichiometry). The defective nature of these structures is well demonstrated by the broad peaks in their diffraction patterns, indicative of a propensity towards short-range, local ordering, rather than long-range ordering. Substitution of Zr^{4+} with Ru^{4+} resulted in a slight lattice contraction, which increased with the extent of substitution. The lattice parameter decreased from 5.201 Å for $x = 0.0$ to 5.196 Å for $x = 0.2$ (Fig. 2b and Table S10†). This observation is consistent with the smaller ionic radius of Ru^{4+} compared to Zr^{4+} when occupying the same coordination sites within the lattice. Interestingly, additional low intensity peaks characteristic of the C-type phase observed by Naeem et al. in the powder diffraction patterns of $Sm_2Ce_{2-x}Ru_xO_7$,[30] were not observed here, suggesting the absence of such a phase.

SEM (Fig. 3a and b) and TEM (Fig. 3c and d) micrographs give some insight into the micro- and nanoscale structure of synthesised $Y_2Zr_{1.8}Ru_{0.2}O_7$. Large agglomerates, with
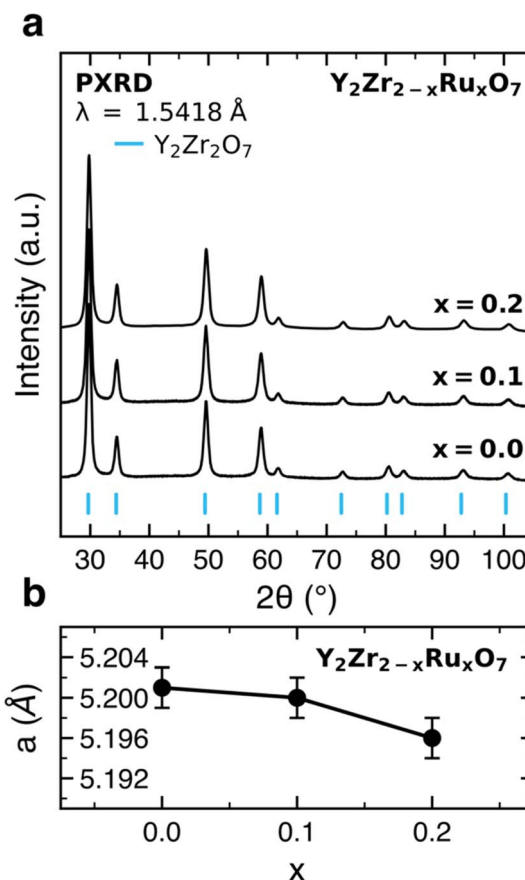

Fig. 2 (a) X-ray powder diffraction patterns ($\lambda = 1.5418$ Å) of synthesised $Y_2Zr_{2-x}Ru_xO_7$ ($x = 0, 0.1, 0.2$), with peaks indexed to ICDD PDF 01-081-8080 ($Y_2Zr_2O_7$, space group $Fm\bar{3}m$).[34] (b) Calculated lattice parameter as a function of substitution level, with error bars representing $\pm 1\sigma$.

dimensions on the order of 1–10 μm, appear to consist of very fine particles, with diameters on the order of 10s of nm. HAADF-STEM (Fig. 3e) and STEM-EDX (Fig. 3f–i) performed on a portion of one of these agglomerates revealed that a high degree of nano-scale porosity is achieved with the citrate sol–gel method that was used, highlighted by the absence of Y, Zr, Ru and O signals in a number of regions. Outside of these pore regions, Y, Zr, Ru and O each appear to be homogeneously distributed throughout the structure, confirming that a phase-pure solid solution of our synthesised material has been obtained. This structure thus appears to allow enhanced compositional tunability compared to simple fluorite matrices, for which the solubility of transition metals is often limited.[24]

Probing the effects of composition, temperature and time

In order to probe how the different processing parameters in a standard reduction treatment (time, temperature, dopant concentration) govern exsolution in this system, ex situ XPS measurements were performed on $Y_2Zr_{2-x}Ru_xO_7$ samples with different Ru substitution levels ($x = 0.1, 0.2$) reduced at a series of reduction temperatures (400–1000 °C, in intervals of 100 °C) for a fixed duration (6 h). The acquired XPS Ru 3d core level

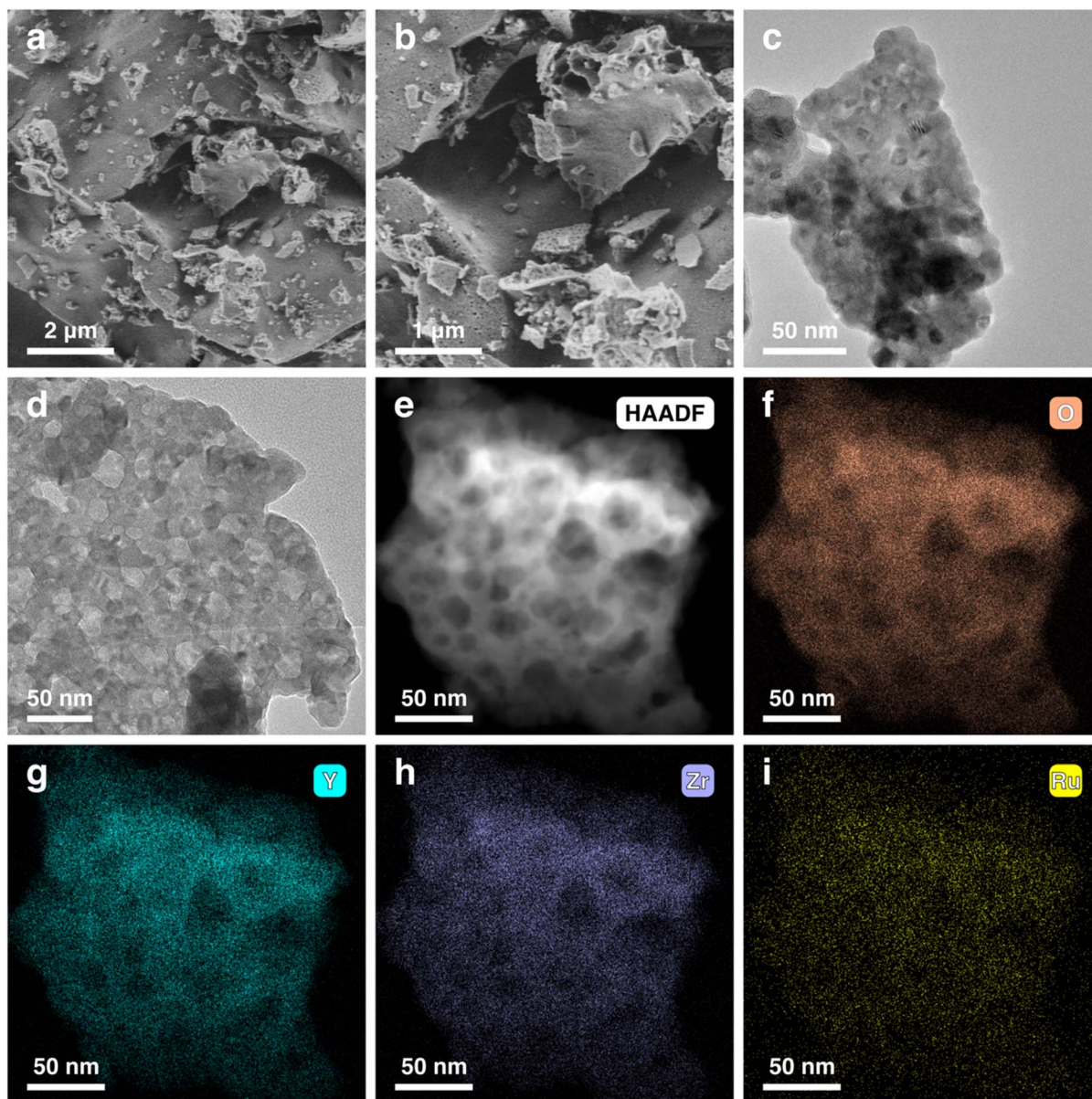This journal is © The Royal Society of Chemistry 2025

J. Mater. Chem. A, 2025, 13, 6451–6468 | 6455

Fig. 3 SEM (a) and (b), TEM (c) and (d) and STEM-EDX (e)–(i) images of synthesised $Y_2Zr_{1.8}Ru_{0.2}O_7$.

spectra for both compositions are plotted in Fig. 4, while the relative atomic percentages calculated for spectra acquired at each reduction temperature are plotted in Fig. 5.

Before discussing our interpretation of the measured spectra, it is worth briefly outlining some of the challenges that can complicate interpretation of the Ru 3d core level spectrum. The first is direct overlap with the C 1s core level. Unless adventitious carbon is completely removed from the sample, it is likely that it will contribute somewhat to the overall signal. The second is the complex satellite structures observed in a number of ruthenium compounds (e.g., RuO_2, $Bi_2Ru_2O_7$, $SrRuO_3$).[41,42] These satellite structures can manifest in a similar manner to multiple different Ru oxidation states, when in reality their origin lies in final state effects during the photoemission process.[43] Thus, when making peak attributions in the

Ru 3d core level, it is important to carefully consider whether a peak results from an initial state effect (e.g., a different oxidation state) or a final state effect.

In our peak fitting model, the Ru 3d core level XPS spectra of $Y_2Zr_{1.8}Ru_{0.2}O_7$ are fitted with a series of four doublets. In order from low to high binding energy, these doublets are attributed to Ru^0 (metallic ruthenium), Ru^{3+}, Ru^{4+} and Ru^{x+} ($x > 4$). The binding energy scale has been calibrated by setting the Zr $3d_{5/2}$ peak to 181.4 eV (the binding energy measured for both $Y_2Zr_{1.9}Ru_{0.1}O_7$ and $Y_2Zr_{1.8}Ru_{0.2}O_7$ before reduction) to correct for shifts to higher binding energies following reduction. We expect these shifts to result from an upwards shift of the Fermi level towards the vacuum level (correlating to the Fermi level moving closer to the conduction band) observed when electron doping takes place as a result of oxygen vacancy formation under reducing conditions.[44]
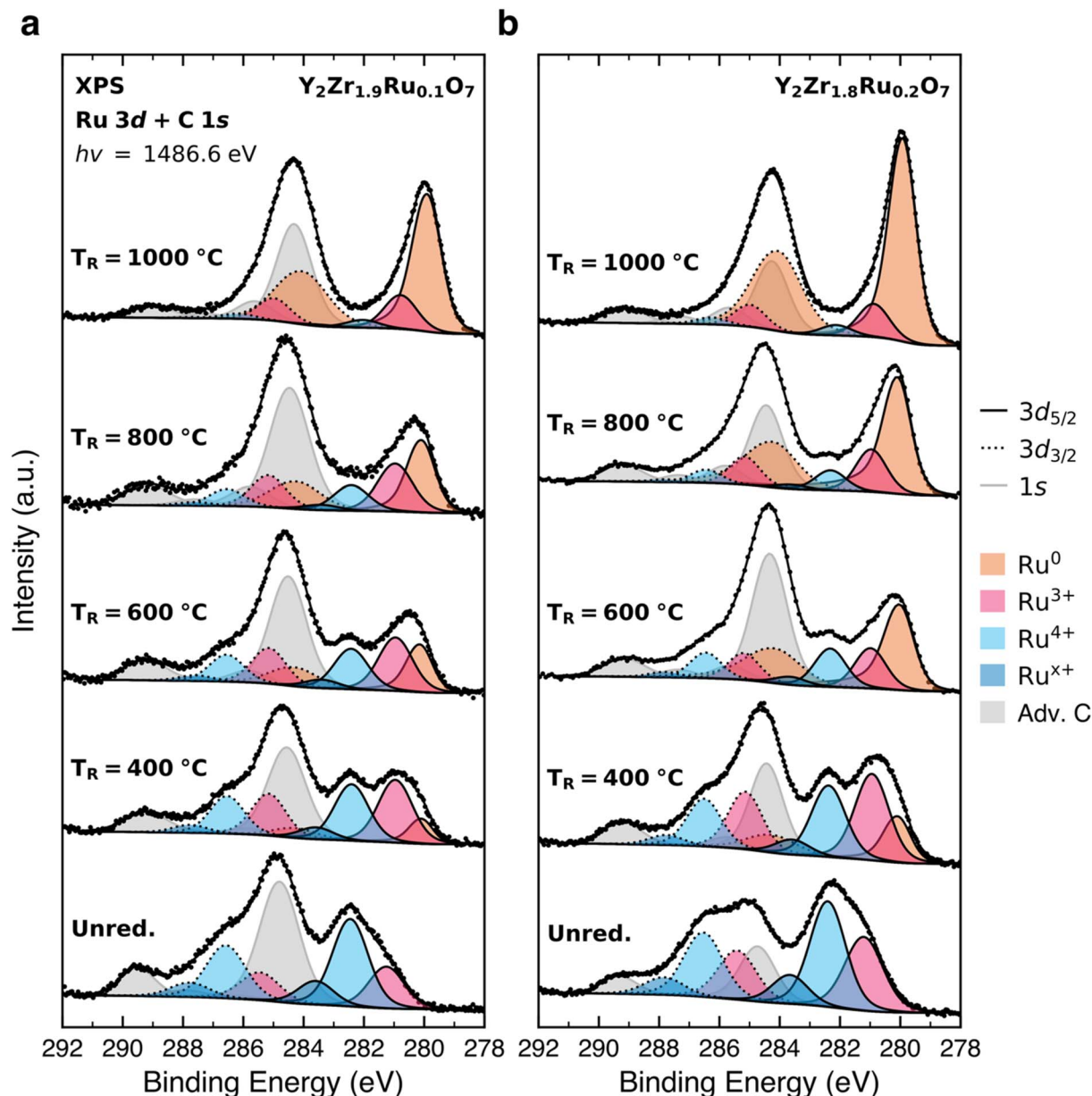
Fig. 4 Ru 3d core level region of the photoelectron spectra of $Y_2Zr_{1.9}Ru_{0.1}O_7$ (a) and $Y_2Zr_{1.8}Ru_{0.2}O_7$ (b) as a function of reduction temperature (T_R = 400, 600, 800, 1000 °C), with measurements before reduction included as a reference. All reduction procedures consisted of a 6 h isothermal hold at the specified temperature under flowing 5% H_2/N_2, with a 5 °C min^{-1} ramp rate.

It is fairly straightforward to assign the lowest binding energy doublet to Ru^0, owing to the close proximity of its $3d_{5/2}$ component to that of a Ru powder reference (Fig. S1a†) at ~284.0 eV. This doublet appears following reduction at temperatures as low as 400 °C (the lowest temperature investigated *ex situ*) and exhibits a clear increase in intensity as the reduction temperature is increased. This matches well to previous XPS measurements of exsolved materials as a function of reduction temperature, which show a clear increase in the extent of reduction to a metallic state as the reduction temperature increases.[45]

Proceeding towards higher binding energies, the next doublet has a $3d_{5/2}$ component centred at 281 eV and is

tentatively assigned to Ru^{3+}. This doublet is present in the as-synthesised sample before any reductive treatment, increases in intensity following reduction at 400 °C, then gradually decreases in intensity as the reduction temperature is increased, albeit more slowly than the doublets at higher binding energies. The chemical state giving rise to this doublet should therefore be stable under ambient conditions (before any reductive treatment) and is expected to be some intermediate in the reduction of Ru^{4+} to Ru^0. One possibility is a secondary phase of RuO_2, the $3d_{5/2}$ component of which also lies close to 281 eV (Fig. S1b†). However, several observations suggest that this doublet cannot be solely attributed to a secondary phase of RuO_2. Firstly, its intensity increases
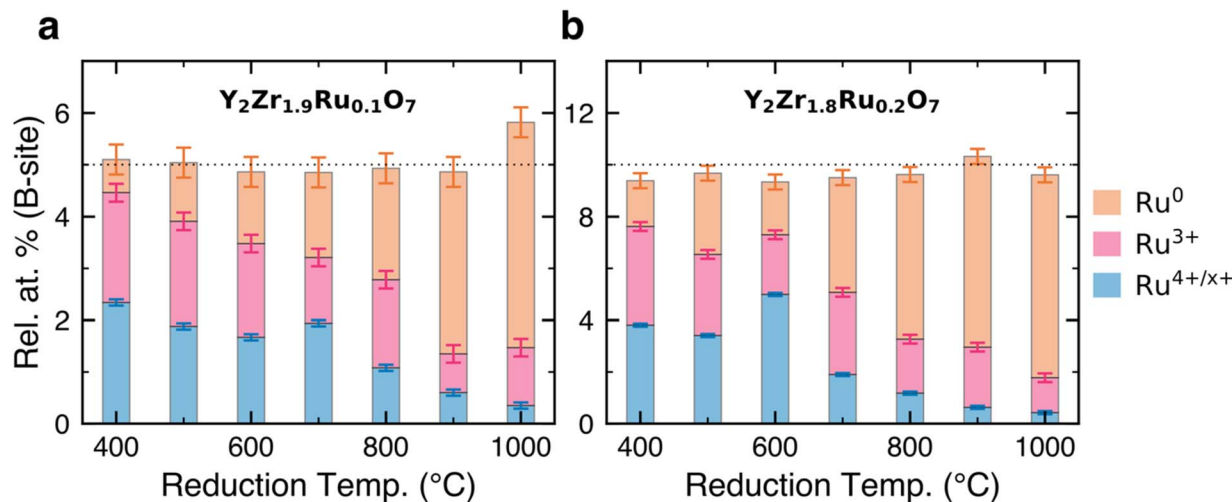
This journal is © The Royal Society of Chemistry 2025

J. Mater. Chem. A, 2025, **13**, 6451–6468 | **6457**

Fig. 5 Relative atomic percentages of the different components of the Ru 3d core level region of $Y_2Zr_{1.9}Ru_{0.1}O_7$ (a) and $Y_2Zr_{1.8}Ru_{0.2}O_7$ (b) as a function of reduction temperature. The horizontal dotted lines at 5 at% (a) and 10 at% (b) represent the nominal doping concentration. Error bars were calculated by taking the average of the standard error calculated for three repeat measurements performed on $Y_2Zr_{1.8}Ru_{0.2}O_7$ samples reduced at 600, 700, 800 and 900 °C.

following reduction at 400 °C. This is contrary to what is expected for RuO_2, the formation of which is unfavourable under reducing conditions. Secondly, the doublet exhibits a symmetric peak shape rather than the asymmetric shape expected for RuO_2, and lacks its characteristic satellite. Finally, no secondary phase peaks were observed in the PXRD pattern of the as-synthesised samples (Fig. 2). While a small amount of RuO_2 below the detection limit of XRD might exist, and therefore may contribute to some degree towards the Ru 3d core level spectrum, it is unlikely to be the primary contributor towards the doublet observed in this region of the Ru 3d core level spectrum. Lower oxidation states than Ru^{3+} also seem unlikely; although Ru^{2+} has been observed at binding energies close to 281 eV in certain complexes and transition metal dichalcogenides,[46,47] it has not been commonly observed in oxides. On the other hand, it is plausible that Ru^{3+} could be present under ambient conditions in regions that show some degree of oxygen deficiency, or possibly as a result of substitution for Y^{3+} rather than Zr^{4+}. Under mildly reducing conditions, the concentration of Ru^{3+} would be expected to increase as the lattice becomes more oxygen deficient and reduction from Ru^{4+} to Ru^{3+} compensates for positively charged oxygen vacancy defects. Under more extreme reducing conditions, the concentration of Ru^{3+} would eventually decrease, as reduction from Ru^{3+} to Ru^0 becomes progressively more favourable.

The next doublet (with its $3d_{5/2}$ component centred at 282.5 eV) is assigned to Ru^{4+}. The intensity of this doublet is at its highest before reduction, then progressively decreases as the reduction temperature is increased, effectively disappearing following reduction at 1000 °C. With this doublet representing the chemical state with the highest concentration before reduction, and demonstrating a progressive decrease in concentration following reduction at higher temperatures, it appears reasonable to attribute this doublet to the expected oxidation state of Ru^{4+} substituting for Zr^{4+}. The assignment of

this doublet to Ru^{4+} is supported by similar binding energy positions observed for the Ru $3d_{5/2}$ component of Ru^{4+} compounds in a number of previous works.[48,49]

The highest binding energy doublet, with its $3d_{5/2}$ component centred at 283.7 eV, is more challenging to confidently assign. From our NAP-XPS measurements (Fig. 6) we observe that this doublet increases significantly in intensity under oxidising conditions, where a lower oxygen vacancy concentration is expected. Such behaviour can be explained by attributing this doublet to a higher oxidation state of ruthenium, the concentration of which would be expected to increase under oxidising conditions. As this doublet is present in the as-synthesised sample, this state of ruthenium must be stable under ambient conditions, possibly in regions that show some degree of oxygen excess. However, assigning this doublet to a specific oxidation state is complicated by the fact that Ruthenium has been observed in a number of higher oxidation states. Ru^{5+} is stable in some compounds with the closely related pyrochlore structure (e.g., $Cd_2Ru_2O_7$, $Hg_2Ru_2O_7$),[50,51] while XPS studies of oxidised ruthenium metal surfaces have provided evidence for the existence of Ru^{6+} and Ru^{8+} in RuO_3 and RuO_4, respectively.[52] Owing to the difficulty in isolating these oxidation states, their binding energies are poorly defined and not completely consistent. As such, to avoid being too speculative around the exact nature of this peak, we assign this doublet to Ru^{x+}, where $x+$ refers to some oxidation state higher than 4+.

In our analysis so far, we have fitted the complex Ru 3d core level spectra with four doublets, and attributed these solely to initial state effects – different oxidation states, the relative intensity of which depends on the treatment conditions. However, final state screening effects have been observed in various ruthenates, and these can also lead to complex line shapes.[41] Final state screening results in a given chemical state of ruthenium exhibiting two doublets rather than one: a well-screened doublet at lower binding energies and a poorly-
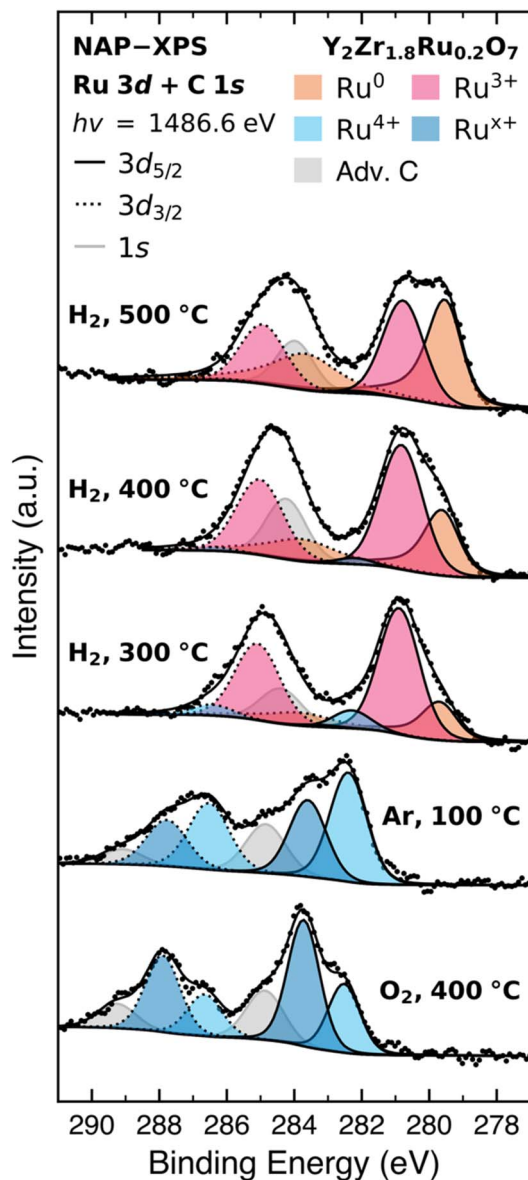
6458 | *J. Mater. Chem. A*, 2025, **13**, 6451–6468

This journal is © The Royal Society of Chemistry 2025

Fig. 6 *In situ* NAP-XPS measurements of the Ru 3d core level region of the photoelectron spectrum of $Y_2Zr_{1.8}Ru_{0.2}O_7$. Spectra were acquired sequentially under the following series of conditions and averaged over their respective acquisition times (t_a): (1) 0.5 mbar O_2, 400 °C, t_a = 100 h (2) 0.5 mbar Ar, 100 °C, t_a = 80 h (3–5) 0.5 mbar H_2, 300–500 °C, t_a = 60 h.

screened doublet at higher binding energies, separated by approximately 2 eV.[41] These doublets typically exhibit different line shapes as a result of the distinct physical processes involved in the two final states.[53] Their relative intensity and separation will depend, among other factors, on the carrier concentration, which itself will depend on the composition and processing history of the material. An increase in the carrier concentration leads to a decrease in the intensity of the poorly-screened doublet relative to the well-screened doublet, and an increase in the separation between the doublets.[54,55] Although it is difficult to entirely discount the possibility of contributions

from final state screening effects in our analysis of the Ru 3d core level, the uniform line shapes of the fitted components and their fixed separation over the range of conditions tested lead us to believe that the Ru 3d core level spectra are best interpreted as comprising doublets arising from initial state effects, specifically different oxidation states of ruthenium, rather than final state effects. Nonetheless, we remain hesitant to completely discount the possibility of any contributions from final state effects. We will seek to identify any such contributions in future work by employing advanced spectroscopic techniques capable of distinguishing them from initial state effects.

With the observed doublets attributed to ruthenium in a series of different oxidation states, the XPS measurements of the *ex situ* reduction series plotted in Fig. 4 and 5 present a few noteworthy results. Firstly, it is clear that complete reduction of all substituted ruthenium to metallic ruthenium does not take place following any of the treatments that have been performed, suggesting that more extreme conditions (higher temperature, lower pO_2 or an extended reduction time) are required to fully exsolve all substituted ruthenium, and that reduction, or a process prior to reduction, may be the limiting step governing the extent of exsolution in this system.

While there is a clear positive correlation between Ru^0 concentration and reduction temperature when pO_2 and reduction time are held constant, further investigation of the relationship between the extent of reduction and reduction temperature is complicated by the fact that the equilibrium extent of exsolution at a given temperature has not necessarily been reached within the time frame of our reductive treatment. Comparison of $Y_2Zr_{1.9}Ru_{0.1}O_7$ after reduction at 800 °C for 6 hours and 12 hours (Fig. S2†) reveals a clear increase in the extent of reduction with a longer reduction time, indicative of a kinetic limit on reduction over the timescale of hours under these conditions. Therefore, the measured spectra do not necessarily represent equilibrium at a given temperature, but rather the extent of reduction that took place within the time frame of reduction at that temperature.

Contrasting the positive correlation between Ru^0 concentration and reduction temperature, the concentrations of both $Ru^{4+/x+}$ and Ru^{3+} exhibit a negative correlation. The concentration of $Ru^{4+/x+}$ appears to decrease at a faster rate than Ru^{3+}, and is almost fully depleted following reduction at 1000 °C, while a considerable amount of Ru^{3+} remains. One explanation for such behaviour could be a stepwise reduction mechanism, with an intermediate reduction step to Ru^{3+} preceding complete reduction to Ru^0.

Comparison of the relative proportions of Ru^0, Ru^{3+} and $Ru^{4+/x+}$ as a function of temperature between $Y_2Zr_{2-x}Ru_xO_7$ with $x = 0.1$ and 0.2 (Fig. 5), reveals that they are fairly similar at most temperatures. Although the absolute amount of exsolved metallic ruthenium is greater in the sample with $x = 0.2$, the relative proportion of exsolved metallic ruthenium at a given temperature does not vary significantly with substitution level. Therefore, a lower doping concentration may not necessarily improve utilisation of the active component by guaranteeing complete exsolution at a lower temperature or with a shorter

This journal is © The Royal Society of Chemistry 2025

J. Mater. Chem. A, 2025, **13**, 6451–6468 | **6459**

reduction time. It is also interesting to note that the total amount of ruthenium relative to zirconium remains effectively constant over the range of reduction temperatures. This suggests that no additional ruthenium is being drawn from outside of the probing depth ($\sim$10 nm for the Al Kα X-ray source). One explanation for this could be that the host grains are sufficiently small (on the order of 10s of nm) that the surface region probed in our measurements encompasses a significant proportion of the overall volume, limiting the bulk from which additional ruthenium can be drawn. An alternative explanation could be that in this system, under the range of conditions investigated, there is no driving force for additional ruthenium to migrate to the surface region defined by the probing depth of our XPS measurements. The former matches our experimental results well; however, further experiments are required to fully discount the possibility of the latter, and will be the subject of future work.

The XPS O 1s, Zr 3d and Y 3d core level spectra for Y$_2$Zr$_{2-x}$Ru$_x$O$_7$ ($x = 0.1, 0.2$) accompanying the Ru 3d core level spectra plotted in Fig. 4 are plotted in Fig. S3–S5,† respectively. These spectra appear unchanged following the series of reductive treatments applied, with no clear trends observed with increasing reduction temperature. This provides further supporting evidence that the host structure remains intact and largely unaffected following exsolution of ruthenium.

The observed stability of the host ions also suggests that the proposed stepwise reduction mechanism from Ru^{x+} to Ru^0 is localised to the Ru ions, without significant participation from other host ions. Reduction is thus primarily expected to take place via transfer of electrons introduced when oxygen vacancies are created within the lattice, with the extent of reduction, and the stability of intermediate oxidation states of Ru, depending closely on the level of oxygen deficiency, which in turn depends on the reducing conditions applied. While this mechanism provides a potential framework for understanding the reduction process taking place in this system during exsolution, further testing will be required to establish its validity.

Evolution of the chemical state of ruthenium during exsolution

In order to build upon the insights gained through our ex situ XPS measurements discussed in the previous section, as well as to verify the peak fitting model developed based on these measurements, NAP-XPS measurements were performed on a pellet of Y$_2$Zr$_{1.8}$Ru$_{0.2}$O$_7$ under a range of conditions (0.5 mbar O$_2$, 400 °C; 0.5 mbar Ar, 100 °C; and 0.5 mbar H$_2$, 300–500 °C). With acquisition times ranging from 50–100 hours in order to achieve suitable signal-to-noise ratios, we expect the averaged spectra to represent the equilibrium chemical state under each environment. These spectra were fitted with the peak model developed based on our ex situ XPS measurements (Fig. 4) which was found to capture the observed peaks and their relative separations very well.

The acquired NAP-XPS Ru 3d core level spectra are plotted in Fig. 6. As for the ex situ XPS measurements, the binding energy scale has been calibrated by setting the Zr 3d$_{5/2}$ peak to 181.4 eV

to correct for significant shifts to higher binding energies observed under reducing conditions (approximately 0.4 eV under Ar at 100 °C and 1.1 eV under H$_2$ at 300–500 °C). While this calibration method ensures that lattice ruthenium peaks are aligned, it has the unfortunate effect of shifting the metallic ruthenium peak (which exhibits a differential binding energy shift compared to lattice ruthenium, possibly as a result of some degree of Fermi level pinning) to a binding energy approximately 0.4 eV below its expected position at $\sim$284 eV.[42] Similarly, we expect misalignment between the Fermi level of the sample and adventitious carbon under these conditions to result in deviation of the C–C peak of adventitious carbon from its expected position at 284.8 eV. The binding energy positions of the other three doublets (attributed to Ru^{3+}, Ru^{4+} and Ru^{x+} in the host oxide) are expected to be reliable, which is verified by the similarity of their peak positions to those measured ex situ (Fig. 4).

Under highly oxidising conditions (400 °C, 0.5 mbar O$_2$), we see only two doublets – the higher binding energy doublet is attributed to Ru^{x+} (with its 3d$_{5/2}$ component centred at 283.7 eV) and the lower binding energy doublet is attributed to Ru^{4+} (with its 3d$_{5/2}$ component centred at 282.5 eV). Notably, the Ru^{x+} doublet is more intense than the Ru^{4+} doublet under oxidising conditions, supporting our attribution of this doublet to some higher oxidation state of ruthenium, the concentration of which would be expected to increase in the case of oxygen excess under highly oxidising conditions. Under these conditions, it appears to be favourable for substituted Ru to exist solely in the Ru^{x+} and Ru^{4+} oxidation states.

Under mildly reducing conditions (100 °C, 0.5 mbar Ar), the concentration of Ru^{x+} drops considerably, accompanied by a corresponding increase in the concentration of Ru^{4+}, possibly to compensate for some degree of oxygen deficiency introduced under the mild reducing conditions imposed. This provides further supporting evidence that Ru substituted in a defective, fluorite-type Y$_2$Zr$_2$O$_7$ host may exist in a mixture of oxidation states. Further NAP-XPS measurements of such ruthenium-substituted oxides under the range of conditions between our extremely oxidising environment (400 °C, 0.5 mbar O$_2$) and mildly reducing environment (100 °C, 0.5 mbar Ar) are warranted to provide further insight into the nature of the higher oxidation state that we presently attribute to Ru^{x+}.

Upon exposure to more extreme reducing conditions (300 °C, 0.5 mbar H$_2$), the Ru^{x+} doublet disappears, accompanied to a great extent by the Ru^{4+} doublet, which is still present but with a significantly diminished intensity. The two doublets that emerge are those attributed to Ru^{3+} (with its 3d$_{5/2}$ component centred at 281 eV) and Ru^0 (the lowest binding energy doublet, with its 3d$_{5/2}$ component slightly below 280 eV). At temperatures as low as 300 °C under 0.5 mbar H$_2$, we see almost complete reduction of Ru^{4+} to Ru^{3+}, and a small degree of reduction to Ru^0. Under progressively more extreme reducing conditions (400–500 °C, 0.5 mbar H$_2$), the Ru^0 doublet progressively increases in intensity, accompanied by a corresponding decrease in the intensity of the Ru^{3+} doublet.

The acquired NAP-XPS O 1s, Zr 3d and Y 3d core level spectra for Y$_2$Zr$_{1.8}$Ru$_{0.2}$O$_7$ accompanying the Ru 3d core level spectra

6460 | J. Mater. Chem. A, 2025, 13, 6451–6468

This journal is © The Royal Society of Chemistry 2025

plotted in Fig. 6 are plotted in Fig. S6–S8,† respectively. While the peaks attributed to lattice Y^{3+}, Zr^{4+} and O^{2-} remain stable under increasingly reducing conditions, peaks attributed to surface carbonates exhibit a progressive decrease in intensity. This corroborates the trend observed in the Ru 3d core level region, where the C 1s peak attributed to surface carbonates gradually decreases in intensity as the reduction temperature increases, indicating a reduced presence of surface carbonate species.

There are two important take-aways from the NAP-XPS results in Fig. 6. Firstly, it appears that almost complete reduction from Ru^{4+} to Ru^{3+} precedes reduction from Ru^{3+} to Ru^0. Secondly, it appears that the extent of reduction reaches a stable equilibrium at each temperature over the time scale of our measurements (60 hours at each reduction temperature). The former is of interest, as it provides further evidence for a stepwise reduction process in this system, in line with a recent study of ruthenium exsolution from the $LaFe_{0.9}Ru_{0.1}O_3$ perovskite system, where a similar evolution of the chemical state of ruthenium was observed.[56] The latter provides valuable insight into the factors limiting the extent of reduction (and thus, the extent of exsolution) in this system. When reduction from Ru^{3+} to Ru^0 is given ample time to reach equilibrium (no further increase in reduction observed with increasing reduction time) at each reduction temperature, it is clear that an equilibrium extent of reduction from Ru^{3+} to Ru^0 is reached, which increases with temperature. This suggests that the extent of reduction in this system may not solely be limited by sluggish kinetics at low temperatures, resulting in a rate that prevents complete exsolution over a reasonable timescale. Rather, there may be a limit on the extent of reduction that can take place at a given temperature and partial pressure of oxygen, independent of the timescale of reduction. This could have important implications for the design of exsolution treatments, suggesting that considerations of the kinetics of exsolution (reducing for a sufficient time period to reach the equilibrium extent of reduction) should be accompanied by considerations of possible limitations on the extent of exsolution (reducing at sufficiently high temperatures or low partial pressures of oxygen to maximise the equilibrium extent of reduction). Based on our results, this may provide a unique and valuable opportunity to carefully tailor of the extent of exsolution in this system over accessible temperature ranges and timescales. While a limit on the extent of reduction in this system remains speculative, we believe the evidence towards such a limitation outlined in this work warrants further investigation in order to fully understand the factors governing the extent of exsolution, thereby better informing the design of reductive treatments.

Exsolved $Y_2Zr_{2-x}Ru_xO_7$ for the reverse-water-gas-shift reaction

Based on the preceding XPS measurements, in which reduction at 1000 °C resulted in the highest proportion of metallic ruthenium, $Y_2Zr_{1.8}Ru_{0.2}O_7$-R10 (reduced at 1000 °C for 6 h) was chosen for preliminary catalytic testing, in order to evaluate the applicability of our newly designed systems. The reverse-water-gas-shift reaction was chosen as a proof of concept for this

catalyst based on its significance as one of the most important applications in the process industry and a present side reaction in many applications. The $x = 0.2$ composition was selected over the $x = 0.1$ composition to more closely match typical levels of active metal loading in ruthenium-based catalysts.[57–59]

PXRD patterns of $Y_2Zr_{2-x}Ru_xO_7$-R10 ($x = 0.0, 0.1, 0.2$) (Fig. 7a) continue to demonstrate a close match to cubic $Y_2Zr_2O_7$ (space group $Fm\overline{3}m$) in PDF 01-081-8080;[34] however, additional peaks emerge for $Y_2Zr_{1.8}Ru_{0.2}O_7$-R10 that are not visible for $Y_2Zr_2O_7$-R10. A closer view of the 37–47° 2θ region (Fig. 7b) reveals three broad peaks at 38.4, 42.2 and 44.1° 2θ that match closely to reflections from the (100), (002) and (101) planes, respectively, of hcp Ru metal (space group $P6_3/mmc$) in PDF 00-006-0663.[34] This provides corroborative evidence that the reductive treatment applied was successful in exsolving Ru, while leaving the host structure intact. The absence of these peaks in the case of $Y_2Zr_{1.9}Ru_{0.1}O_7$-R10 may be due to the amount of exsolved Ru being below the detection limit of the diffractometer. A closer view of the 97–104° 2θ region (Fig. 7c) reveals the difference in position of the highest angle $Y_2Zr_{2-x}Ru_xO_7$-R10 peak between compositions. As the substitution level of ruthenium increases, there is a greater extent of lattice expansion relative to before reduction (Fig. 7g). This is attributed to an increase in the number of vacant sites introduced when a larger proportion of ruthenium is substituted and subsequently exsolved.

PXRD patterns of $Y_2Zr_{1.8}Ru_{0.2}O_7$ as a function of reduction temperature (Fig. 7d) accompanied by closer views of the 37–47° 2θ region (Fig. 7e) and 97–104° 2θ region (Fig. 7f) suggest that exsolved Ru only reaches a detectable amount following reduction at 1000 °C; however, the extent of lattice expansion relative to before reduction can be seen to progressively increase with increasing reduction temperature (Fig. 7h). This provides corroborating evidence that the extent of exsolution increases with increasing reduction temperature as more ruthenium is exsolved and consequently a greater number of vacancies are introduced, resulting in a slightly higher degree of expansion of the host lattice.

SEM micrographs (Fig. 8a and b) of $Y_2Zr_{1.8}Ru_{0.2}O_7$-R10 show a similar microstructure to $Y_2Zr_{1.8}Ru_{0.2}O_7$ before reduction. TEM (Fig. 8c and d) and HAADF-STEM (Fig. 8e) images show a high density of exsolved nanoparticles distributed across the host grains. Further insight into the composition of these particles is gained from the acquired STEM-EDX maps (Fig. 8f–i), which show that Ru is concentrated within the exsolved nanoparticles. Interestingly, Fig. 8f–i show that the largest of the imaged exsolved particles has a diameter of ~20 nm; however, surrounding particles appear to be much smaller, with diameters on the order of a few nm. This suggests the presence of a bimodal size distribution following reduction at 1000 °C. As has been observed in several other systems, one possible explanation for this bimodal size distribution could be secondary nucleation of new particles alongside the growth of early-formed particles during the extended dwell time at a high reduction temperature of 1000 °C. Specifically, wider size distributions indicative of different particle size regimes have been observed after high temperature reduction during both *ex*
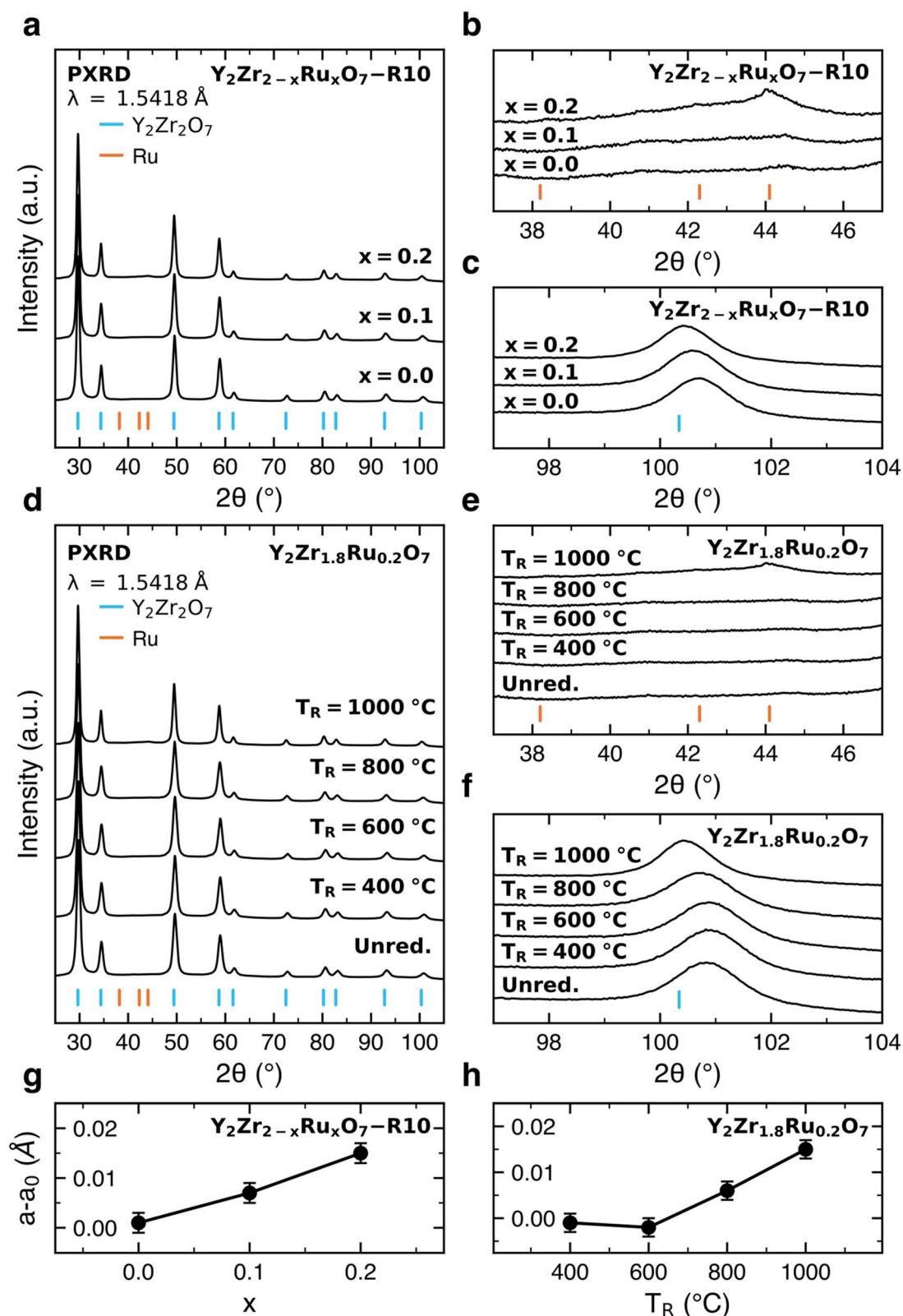
Fig. 7 (a) X-ray powder diffraction patterns (λ = 1.5418 Å) of $Y_2Zr_{2-x}Ru_xO_7$-R10 (x = 0, 0.1, 0.2), with a closer view of (b) main peaks of Ru metal and (c) highest angle peak of $Y_2Zr_{2-x}Ru_xO_7$. (d) X-ray powder diffraction patterns of $Y_2Zr_{1.8}Ru_{0.2}O_7$ and $Y_2Zr_{1.8}Ru_{0.2}O_7$-Rxx (xx = 04, 06, 08, 10), with a closer view of (e) main peaks of Ru metal and (f) highest angle peak of $Y_2Zr_{2-x}Ru_xO_7$. Peaks are indexed to ICDD PDF 01-081-8080 ($Y_2Zr_2O_7$, space group $Fm\bar{3}m$) and ICDD PDF 00-006-0663 (Ru, space group $P6_3/mmc$). (g) and (h) Difference in lattice parameter before (a_0) and after (a) reduction, plotted against substitution level (g) and reduction temperature (h), with error bars representing $\pm1\sigma$.
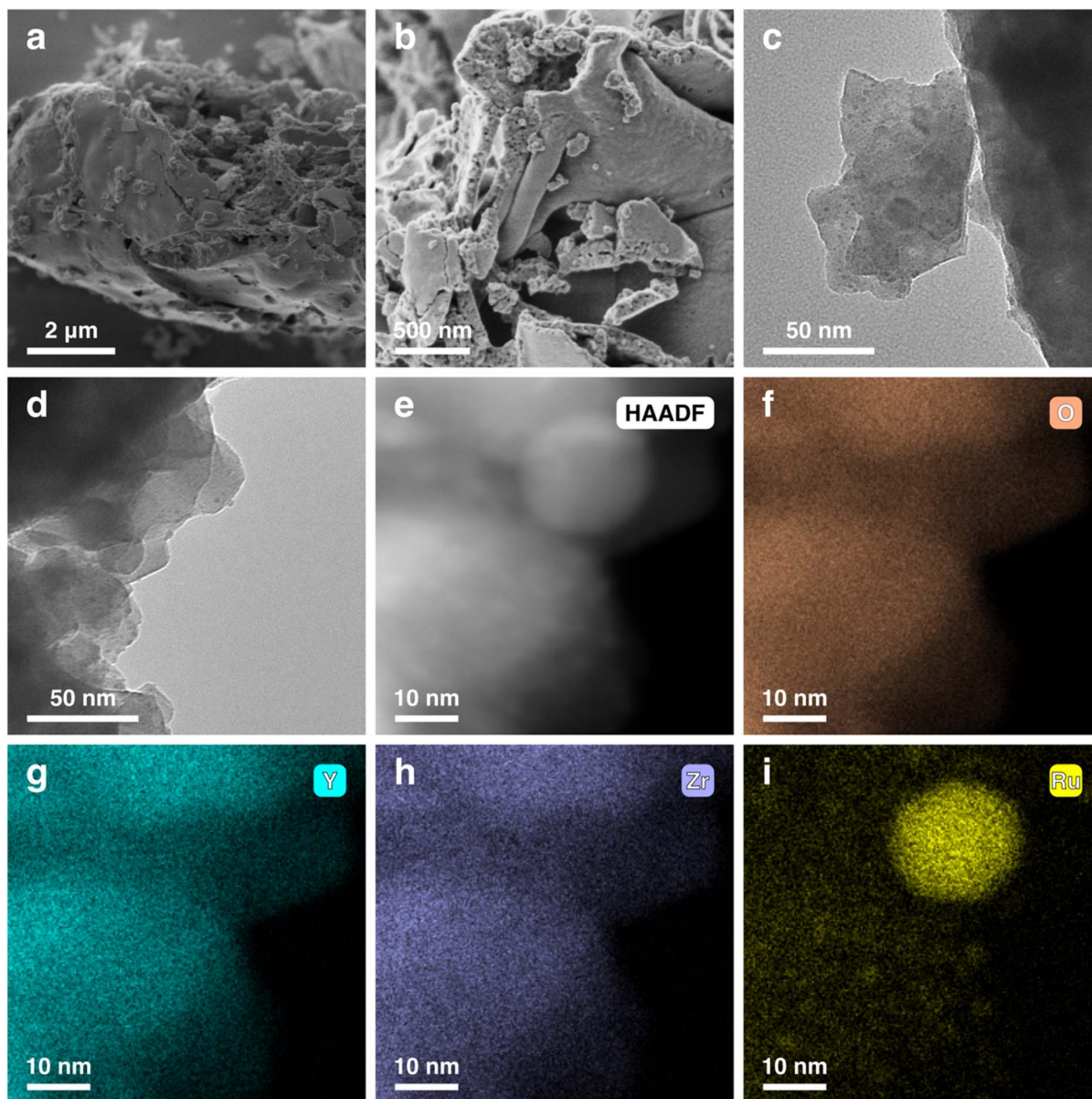
6462 | J. Mater. Chem. A, 2025, 13, 6451–6468

This journal is © The Royal Society of Chemistry 2025

Fig. 8 SEM (a) and (b), TEM (c) and (d) and STEM-EDX (e)–(i) images of $Y_2Zr_{1.8}Ru_{0.2}O_7$-R10 (reduced for 6 h at 1000 °C under flowing 5% H_2/N_2, with a 5 °C min^{-1} ramp rate).

situ and *in situ* microscopy experiments, with the size distribution generally growing broader at higher reduction temperatures.[21,45] Such bimodal size distributions have also been observed in systems that demonstrate exsolution of both surface (exogenous) and bulk (endogenous) nanoparticles;[60,61] investigating whether $Y_2Zr_{2-x}Ru_xO_7$ exhibits the formation of endogenous as well as exogenous nanoparticles is of great interest and will be the scope of future investigation.

To further investigate the trend in exsolved particle size with reduction temperature, size analysis of particles exsolved from $Y_2Zr_{1.8}Ru_{0.2}O_7$ at a series of reduction temperatures ($T_R = 400$, 600, 800 and 1000 °C) (Table S19 and Fig. S10†) was performed by identifying and measuring exsolved particles in a series of TEM images. In order to minimise erroneous particle identification, only particles with diameters exceeding 1 nm contributed towards size analysis, of which an appreciable number were only observed following reduction at 800 °C and 1000 °C. The mean particle diameter after reduction at 800 °C was 1.3 ± 0.7 nm, while that after reduction at 1000 °C was 1.9 ± 0.7 nm. The limited number of particles identified with diameters as large as that observed with STEM-EDX in Fig. 8f–i suggests that such particles are relatively scarce, with the majority exhibiting diameters in the nanometre range. Although precise mean diameters could not be obtained following reduction at 400 °C and 600 °C due to the limited number of particles larger than 1 nm, the absence of these larger particles suggests a sub-nanometre mean diameter after reduction at these lower temperatures. This would present

This journal is © The Royal Society of Chemistry 2025

J. Mater. Chem. A, 2025, **13**, 6451–6468 | **6463**

a subtle trend of increasing exsolved particle size with increased reduction temperature, in line with our XRD, XPS and NAP-XPS results that demonstrate an increase in the proportion of exsolved ruthenium with reduction temperature, which we expect contributes towards growth of early-formed particles, possibly accompanied by secondary nucleation of new particles. Such a trend of increasing exsolved particle size following reduction at higher temperatures is in good agreement with trends observed in previous work;[21,45] however, we note that the trend observed in this work lies within the expected range of natural variation, so we are cautious that further measurements with a larger sample size and more temperature intervals are required to establish this trend with greater confidence.

Specific surface area and porosity measurements performed on $Y_2Zr_{1.8}Ru_{0.2}O_7$ and $Y_2Zr_{1.8}Ru_{0.2}O_7$-R10 (Table S20†) indicate that both the specific surface area and the average pore width decrease slightly following reduction. The average BET surface area measured before reduction was 7.80 ± 0.05 m^2 g^{-1}, while that measured after reduction at 1000 °C was 7.44 ± 0.04 m^2 g^{-1}. Average pore widths were measured to be 19.8 ± 0.3 nm (BJH desorption) and 12.2 ± 0.2 nm (desorption) for $Y_2Zr_{1.8}Ru_{0.2}O_7$, and 17.8 ± 0.8 nm (BJH desorption) and 11.5 ± 0.3 nm (desorption) for $Y_2Zr_{1.8}Ru_{0.2}O_7$-R10, matching well the width of pores observed in STEM-EDX measurements of $Y_2Zr_{1.8}Ru_{0.2}O_7$ (Fig. 3). The slight decrease in average BET surface area and pore width following reduction may be a result of coarsening of both host particles and exsolved ruthenium nanoparticles following high temperature reduction. We anticipate that optimisation of synthesis and reduction conditions to maximise the extent of exsolution while minimising particle growth and coarsening could further enhance the surface area of these materials and ensure that this surface area is maintained following reduction, thereby improving their overall catalytic performance.

Activity and stability during the reverse-water-gas-shift reaction

The $Y_2Zr_{1.8}Ru_{0.2}O_7$-R10 catalyst was tested for its activity towards the reverse-water-gas-shift reaction, measuring CO_2 conversion (Fig. 9a) and its selectivity towards CO and CH_4 (Fig. 9b) over a temperature range of 500–800 °C. To facilitate separate consideration of the catalytic properties of the exsolved catalyst and the support, reference measurements were also performed on $Y_2Zr_2O_7$-R10. The lack of any CO_2 conversion detected for $Y_2Zr_2O_7$-R10 over the measured range of temperatures suggests that metallic ruthenium particles must be present for any CO_2 conversion to take place. However, this is not to say that the support plays no role in the reaction; for many catalysts with reducible oxide supports it has previously been demonstrated that the reverse-water-gas-shift reaction follows a Mars van Krevelen-type redox mechanism, where vacancies in the catalyst support are necessary for the activation of CO_2.[62,63] The CO_2 conversion of $Y_2Zr_{1.8}Ru_{0.2}O_7$-R10 can be seen to increase proportionally with temperature, with a maximum of 45% reached at 800 °C, and lies close to the equilibrium curve predicting maximum feasible conversion for
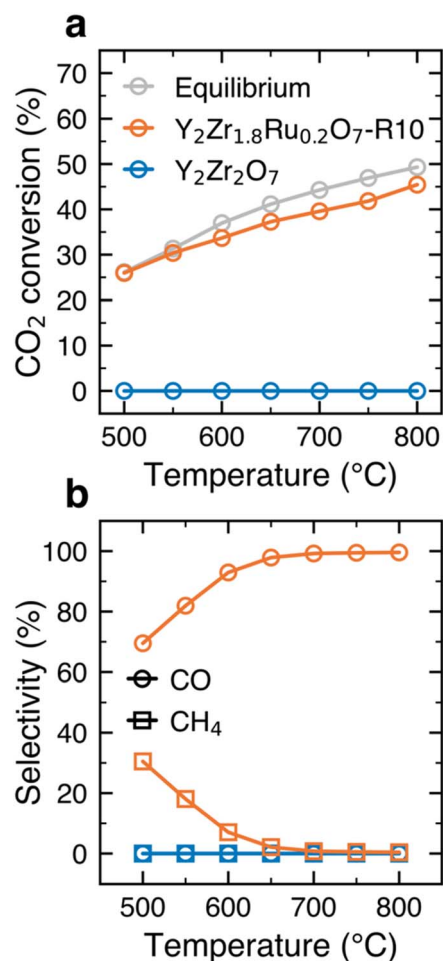

Fig. 9 Catalytic activity measurements of $Y_2Zr_{1.8}Ru_{0.2}O_7$-R10 (reduced for 6 h at 1000 °C under flowing 5% H_2/N_2, with a 5 °C min^{-1} ramp rate) for the reverse water gas shift reaction. (a) The percentage of CO_2 converted compared against equilibrium, and (b) the selectivity of conversion to CO and CH_4, as a function of temperature.

all the tested temperatures. This suggests that our catalyst shows promise in achieving CO_2 conversion efficiencies close to equilibrium.

It is challenging to directly compare CO_2 conversion catalysts, as measurements performed under different conditions will give very different results. For example, the use of higher $H_2:CO_2$ ratios will favour higher conversions by default,[64] but also impacts the economics of the whole process by requiring excessive amounts of H_2.[65] However, when comparing CO_2 conversion at a given temperature with catalysts measured under similar conditions (a 1:1 ratio of $H_2:CO_2$), the $Y_2Zr_{1.8}Ru_{0.2}O_7$-R10 catalyst performs well. Its CO_2 conversion of 26% at 500 °C exceeds that of 2 wt% Pt/mullite (16%) and matches closely that of 2 wt% Pt/2 wt% K/mullite (27%).[66] With the cost of Pt typically exceeding that of Ru more than twofold, the similar performance exhibited by $Y_2Zr_{1.8}Ru_{0.2}O_7$-R10 to Pt-based catalysts highlights its cost-effectiveness. At 600 °C, CO_2 conversion of 34% outperforms those of a number of other Cu–Fe, Cu–Ni and Pd-based catalysts, which demonstrated CO_2 conversions in the range 5–29%.[67–69]
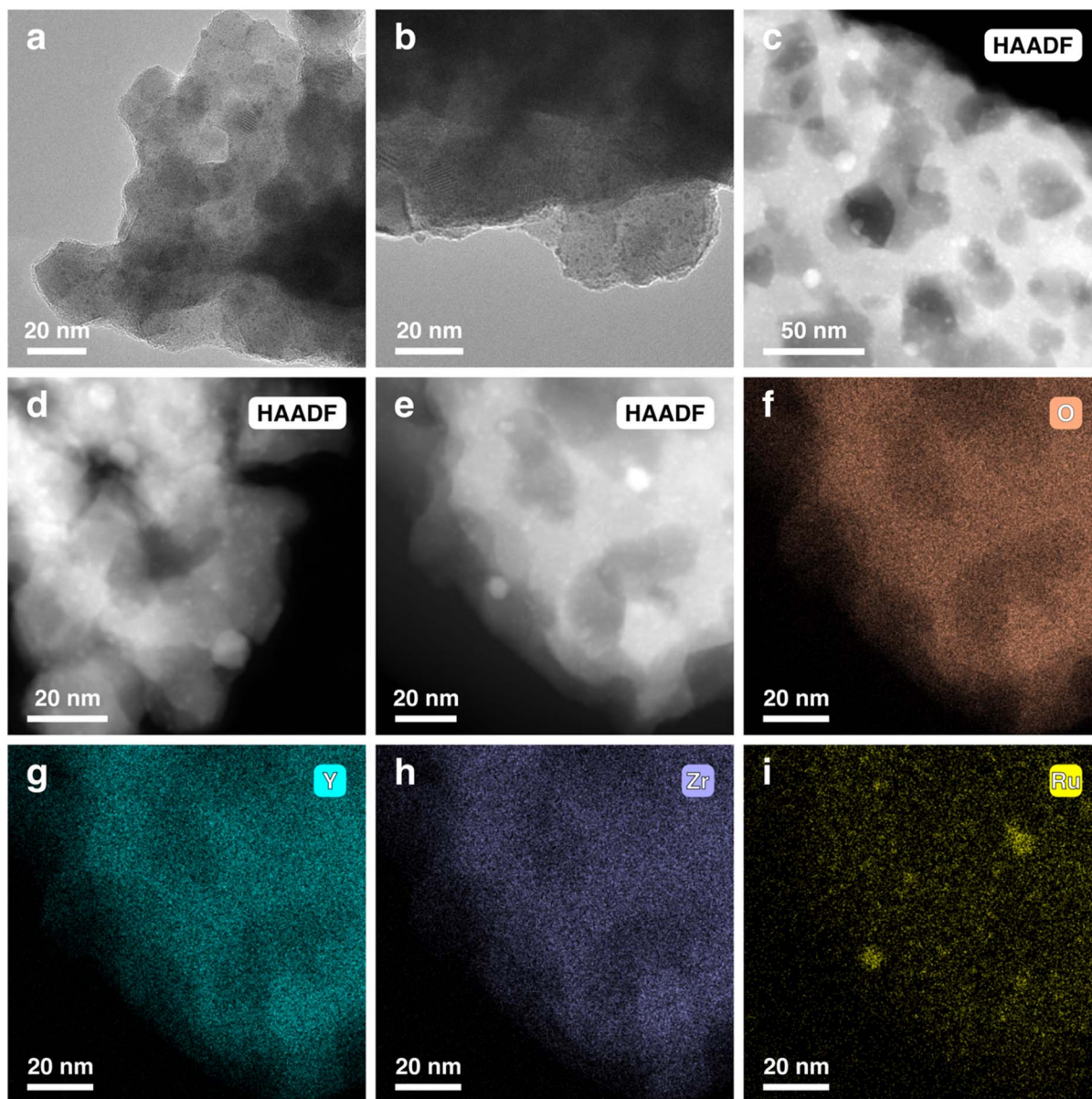
6464 | J. Mater. Chem. A, 2025, 13, 6451–6468

This journal is © The Royal Society of Chemistry 2025

Fig. 10 TEM (a) and (b) and STEM-EDX (c)–(i) images of $Y_2Zr_{1.8}Ru_{0.2}O_7$-R10 following the reverse water gas shift reaction.

The selectivity of $Y_2Zr_{1.8}Ru_{0.2}O_7$-R10 appears to be divided in two different temperature regimes. From 650 to 800 °C, the catalyst achieves 100% selectivity towards CO, which is promising for its application as a high-temperature reverse-water-gas-shift catalyst. At temperatures below 650 °C, the methanation reaction begins to take place; this is not surprising, as ruthenium-based catalysts have long been employed as state-of-the-art methanation catalysts.[70] However, this does highlight the potential applicability of $Y_2Zr_{1.8}Ru_{0.2}O_7$-R10 for different hydrogenation reactions at lower temperatures. As the size of Ru nanoparticles greatly influences their selectivity, the ability to control nanoparticle size through a tailored exsolution process could provide a route to fine tuning of catalyst selectivity through size engineering.[71,72] Comparing the selectivity of our catalyst to CO at 600 °C against iron-, copper-, nickel- and

molybdenum-based catalysts tested under similar conditions, the CO selectivity of 93% observed for $Y_2Zr_{1.8}Ru_{0.2}O_7$-R10 exceeds that of all comparison catalysts, which demonstrated selectivities in the range 35–85%.[69,73,74]

Finally, post-testing characterisation of the $Y_2Zr_{1.8}Ru_{0.2}O_7$-R10 catalyst with XPS (Fig. S6†), TEM (Fig. 10a and b) HAADF-STEM (Fig. 10c–e) and STEM-EDX (Fig. 10f–i) was performed to verify the stability of this catalyst. Our results show that the material does not present any sign of deactivation through NP agglomeration and/or poisoning, with no observable difference in the size and dispersion of exsolved ruthenium nanoparticles or the porous structure compared to before testing (Fig. 8e). No clear changes in the Ru 3d core level that could be associated with a change in chemical state of ruthenium were observed in the post catalytic testing XPS measurements (Fig. S6†),

providing further supporting evidence that the metallic ruthenium nanoparticles remained stable during testing. Although further tests with longer time on-stream are required, these results provide promising evidence that these catalysts are stable and resistant to degradation under reaction conditions.

Conclusions

In this work, we have demonstrated the successful exsolution of metallic ruthenium nanoparticles from a defective, fluorite-type yttrium zirconate host structure and further demonstrated the potential of defect fluorite structures as substrates for exsolved catalysts. X-ray photoelectron spectroscopy measurements performed under vacuum and near-ambient pressure conditions provide insight into the evolution of the chemical state of ruthenium substituents as exsolution progresses, and point towards stepwise reduction from higher oxidation states before eventual reduction to metallic ruthenium. These measurements also suggest the presence of a limit on the extent to which reduction to metallic ruthenium can take place at a given temperature and partial pressure of oxygen. This may have important implications for the design of exsolution treatments, possibly favouring shorter durations under more extreme reducing conditions. These findings highlight the value in systematically employing both *in situ* and *ex situ* XPS techniques to characterise exsolution from a given system, as these techniques are unique in giving us information on the distribution of chemical states as a function of reducing conditions, providing insight into the proportion of the active component that has been reduced, but also, critically, the proportion that has not been reduced. Further characterisation with STEM-EDX indicates that the unique, nanoporous morphology of the host structure is maintained following reduction, after which an extensive distribution of metallic ruthenium nanoparticles is observed. Preliminary evaluation of this exsolved system as a catalyst toward the reverse-water-gas-shift is promising, with our catalyst achieving CO_2 conversion efficiencies close to equilibrium, and 100% selectivity towards CO at temperatures above 650 °C.

Data availability

Additional details of the methodology, results and discussion are available in the ESI† file accompanying this paper. Data contributing towards the findings of this study are openly available at **https://doi.org/10.5281/zenodo.14543374**.

Author contributions

William S. J. Skinner: conceptualisation; investigation; data curation; formal analysis; methodology; writing – original draft. Eleonora Calì: investigation; data curation; formal analysis; methodology; writing – original draft. Angelos Bonis: investigation; data curation; formal analysis; methodology; writing – original draft. Gwilherm Kerherve: formal analysis; methodology; writing – review and editing. Kalliopi Kousi: methodology, funding acquisition; resources; writing – review and

editing. David J. Payne: conceptualisation; supervision; project administration; methodology; funding acquisition; resources; writing – review and editing.

Conflicts of interest

There are no conflicts to declare.

Acknowledgements

References

1 J. R. Rostrup-Nielsen, J. Sehested and J. K. Nørskov, *Adv. Catal.*, 2002, **47**, 65–139.

2 M. E. Dry, *Catal. Today*, 2002, **71**(3–4), 227–241.

3 V. S. Marakatti and E. M. Gaigneaux, *ChemCatChem*, 2020, **12**(23), 5838–5857.

4 Y. A. Daza and J. N. Kuhn, *RSC Adv.*, 2016, **6**(55), 49675–49691.

5 P. Kaiser, R. B. Unde, C. Kern and A. Jess, *Chem. Ing. Tech.*, 2013, **85**(4), 489–499.

6 A. T. Bell, *Science*, 2003, **299**(5613), 1688–1691.

7 P. Munnik, P. E. de Jongh and K. P. de Jon, *Chem. Rev.*, 2015, **115**(14), 6687–6718.

8 H. S. Whang, J. Lim, M. S. Choi, J. Lee and H. Lee, *BMC Chemical Engineering*, 2019, **1**, 9.

9 S. Kattel, P. Liu and J. G. Chen, *J. Am. Chem. Soc.*, 2017, **139**(29), 9739–9754.

10 M. D. Porosoff, B. Yan and J. G. Chen, *Energy Environ. Sci.*, 2015, **9**(1), 62–73.

11 C. H. Bartholomew, *Appl. Catal., A*, 2001, **212**(1–2), 17–60.

12 J. T. S. Irvine, J. L. M. Rupp, G. Liu, X. Xu, S. Haile, X. Qian, A. Snyder, R. Freer, D. Ekren, S. Skinner, O. Celikbilek, S. Chen, S. Tao, T. H. Shin, R. O'Hayre, J. Huang, C. Duan, M. Papac, S. Li, V. Celorrio, A. Russell, B. Hayden, H. Nolan, X. Huang, G. Wang, I. Metcalfe, D. Neagu and S. Garcia Martín, *JPhys Energy*, 2021, **3**(3), 031502.

13 D. Neagu, J. T. S. Irvine, J. Wang, B. Yildiz, A. K. Opitz, J. Fleig, Y. Wang, J. Liu, L. Shen, F. Ciucci, B. A. Rosen, Y. Xiao, K. Xie, G. Yang, Z. Shao, Y. Zhang, J. Reinke, T. A. Schmauss, S. A. Barnett, R. Maring, V. Kyriakou, U. Mushtaq, M. N. Tsampas, Y. Kim, R. O'Hayre, A. J. Carrillo, T. Ruh, L. Lindenthal, F. Schrenk, C. Rameshan, E. I. Papaioannou, K. Kousi, I. S. Metcalfe, X. Xu and G. Liu, *JPhys Energy*, 2023, **5**(3), 031501.

14 D. Neagu, T.-S. Oh, D. N. Miller, H. Ménard, S. M. Bukhari, S. R. Gamble, R. J. Gorte, J. M. Vohs and J. T. S. Irvine, *Nat. Commun.*, 2015, **6**, 8120.

6466 | *J. Mater. Chem. A*, 2025, **13**, 6451–6468

This journal is © The Royal Society of Chemistry 2025

15 E. Calì, S. Saini, G. Kerherve, W. S. J. Skinner, I. S. Metcalfe, D. J. Payne and K. Kousi, *ACS Appl. Nano Mater.*, 2024, **7**(16), 18398–18409.

16 D. Neagu, G. Tsekouras, D. N. Miller, H. Ménard and J. T. S. Irvine, *Nat. Chem.*, 2013, **5**, 916–923.

17 O. Kwon, S. Sengodan, K. Kim, G. Kim, H. Y. Jeong, J. Shin, Y.-W. Ju, J. W. Han and G. Kim, *Nat. Commun.*, 2017, **8**, 15967.

18 J. T. S. Irvine, D. Neagu, M. C. Verbraeken, C. Chatzichristodoulou, C. Graves and M. B. Mogensen, *Nat. Energy*, 2016, **1**, 15014.

19 K. Kousi, C. Tang, I. S. Metcalfe and D. Neagu, *Small*, 2021, **17**(21), 2006479.

20 D. Neagu, V. Kyriakou, I.-L. Roiban, M. Aouine, C. Tang, A. Caravaca, K. Kousi, I. Schreur-Piet, I. S. Metcalfe, P. Vernoux, M. C. M. van de Sanden and M. N. Tsampas, *ACS Nano*, 2019, **13**(11), 12996–13005.

21 E. Calì, M. P. Thomas, R. Vasudevan, J. Wu, O. Gavalda-Diaz, K. Marquardt, E. Saiz, D. Neagu, R. R. Unocic, S. C. Parker, B. S. Guiton and D. J. Payne, *Nat. Commun.*, 2023, **14**, 1754.

22 Y. Gao, D. Chen, M. Saccoccio, Z. Lu and F. Ciucci, *Nano Energy*, 2016, **27**, 499–508.

23 A. Bonkowski, M. J. Wolf, J. Wu, S. C. Parker, A. Klein and R. A. De Souza, *J. Am. Chem. Soc.*, 2024, **146**(33), 23012–23021.

24 A. J. Carrillo, A. López-García, B. Delgado-Galicia and J. M. Serra, *Chem. Commun.*, 2024, **60**(62), 7987–8007.

25 R. T. Parayil, S. K. Gupta, R. Rohilla, J. Prakash, K. Sudarshan and M. Mohapatra, *ACS Appl. Electron. Mater.*, 2023, **5**(9), 5151–5163.

26 S. Kramer, M. Spears and H. L. Tuller, *Solid State Ionics*, 1994, **72**, 59–66.

27 J. Xu, R. Xi, X. Xu, Y. Zhang, X. Feng, X. Fang and X. Wang, *J. Rare Earths*, 2020, **38**(8), 840–849.

28 M. A. Subramanian, G. Aravamudan and G. V. Subba Rao, *Prog. Solid State Chem.*, 1983, **15**(2), 55–143.

29 F. Zhong, J. Zhao, L. Shi, Y. Xiao, G. Cai, Y. Zheng and J. Long, *Sci. Rep.*, 2017, **7**, 4684.

30 M. A. Naeem, P. M. Abdala, A. Armutlulu, S. M. Kim, A. Fedorov and C. R. Müller, *ACS Catal.*, 2019, **10**(3), 1923–1937.

31 Z. Haijun, J. Xiaolin, Y. Yongjie, L. Zhanjie, Y. Daoyuan and L. Zhenzhen, *Mater. Res. Bull.*, 2004, **39**, 839–850.

32 P. Vaqueiro and M. A. López-Quintela, *Chem. Mater.*, 1997, **9**, 2836–2841.

33 T. Degen, M. Sadki, E. Bron, U. König and G. Nénert, *Powder Diffr.*, 2014, **29**, S13–S18.

34 S. Gates-Rector and T. Blanton, *Powder Diffr.*, 2019, **34**(4), 352–360.

35 B. H. Toby and R. B. Von Dreele, *J. Appl. Crystallogr.*, 2013, **46**(2), 544–549.

36 G. Kerherve, A. Regoutz, D. Bentley, C. Hood, K. Feeley, S. Knight, A. Robson, C. Turner, N. Singh, J. Pontefract, J. Åhlund, J. M. Kahk, I. J. Villar-Garcia and D. J. Payne, *Rev. Sci. Instrum.*, 2017, **88**(3), 033102.

37 J. M. Kahk, I. J. Villar-Garcia, L. Grechy, P. J. K. Bruce, P. E. Vincent, S. K. Eriksson, H. Rensmo, M. Hahlin, J. Åhlund, M. O. M. Edwards and D. J. Payne, *J. Electron Spectrosc. Relat. Phenom.*, 2015, **205**, 57–65.

38 M. O. M. Edwards, P. G. Karlsson, S. K. Eriksson, M. Hahlin, H. Siegbahn, H. Rensmo, J. M. Kahk, I. J. Villar-Garcia, D. J. Payne and J. Åhlund, *Nucl. Instrum. Methods Phys. Res., Sect. A*, 2015, **785**, 191–196.

39 S. K. Eriksson, M. Hahlin, J. M. Kahk, I. J. Villar-Garcia, M. J. Webb, H. Grennberg, R. Yakimova, H. Rensmo, K. Edström, A. Hagfeldt, H. Siegbahn, M. O. M. Edwards, P. G. Karlsson, K. Backlund, J. Åhlund and D. J. Payne, *Rev. Sci. Instrum.*, 2014, **85**(7), 075119.

40 J. Schindelin, I. Arganda-Carreras, E. Frise, V. Kaynig, M. Longair, T. Pietzsch, S. Preibisch, C. Rueden, S. Saalfeld, B. Schmid, J.-Y. Tinevez, D. J. White, V. Hartenstein, K. Eliceiri, P. Tomancak and A. Cardona, *Nat. Methods*, 2012, **9**, 676–682.

41 H.-D. Kim, H.-J. Noh, K. H. Kim and S.-J. Oh, *Phys. Rev. Lett.*, 2004, **93**(12), 126404.

42 D. J. Morgan, *Surf. Interface Anal.*, 2015, **47**(11), 1072–1079.

43 P. A. Cox, J. B. Goodenough, P. J. Tavener, D. Telles and R. G. Egdell, *J. Solid State Chem.*, 1986, **83**(2), 360–370.

44 J. Wang, D. N. Mueller and E. J. Crumlin, *J. Eur. Ceram. Soc.*, 2024, **44**(15), 116709.

45 E. Calì, G. Kerherve, F. Naufal, K. Kousi, D. Neagu, E. I. Papaioannou, M. P. Thomas, B. S. Guiton, I. S. Metcalfe, J. T. S. Irvine and D. J. Payne, *ACS Appl. Mater. Interfaces*, 2020, **12**(33), 37444–37453.

46 H. Rensmo, K. Westermark, S. Södergren, O. Kohle, P. Persson, S. Lunell and H. Siegbahn, *J. Chem. Phys.*, 1999, **111**, 2744–2750.

47 Y. Xia, W. Wu, H. Wang, S. Rao, F. Zhang and G. Zou, *Nanotechnology*, 2020, **31**, 145401.

48 M. Jia, Y. Qiao, X. Li, K. Jiang and H. Zhou, *J. Mater. Chem. A*, 2019, **7**, 20405–20413.

49 J. Gaudet, A. C. Tavares, S. Trasatti and D. Guay, *Chem. Mater.*, 2005, **17**(6), 1570–1579.

50 W. Klein, R. K. Kremer and M. Jansen, *J. Mater. Chem. A*, 2007, **17**, 1356–1360.

51 Y. Y. Jiao, J. P. Sun, P. Shahi, Q. Cui, X. H. Yu, Y. Uwatoko, B. S. Wang, J. A. Alonso, H. M. Weng and J.-G. Cheng, *Phys. Rev. B*, 2018, **98**, 075118.

52 H. Y. H. Chan, C. G. Takoudis and M. J. Weaver, *J. Catal.*, 1997, **172**, 336–345.

53 R. G. Egdell, T. J. Walker and G. Beamson, *J. Electron Spectrosc. Relat. Phenom.*, 2003, **128**(1), 59–66.

54 D. J. Payne, R. G. Egdell, D. S. L. Law, P.-A. Glans, T. Learmonth, K. E. Smith, J. Guo, A. Walsh and G. W. Watson, *J. Mater. Chem.*, 2007, **17**, 267–277.

55 R. G. Egdell, J. Rebane, T. J. Walker and D. S. L. Law, *Phys. Rev. B: Condens. Matter Mater. Phys.*, 1999, **59**(3), 1792.

56 Y. Wang, P. Paciok, L. Pielsticker, W. Wang, A. S. Luciano, M. Ding, L. Glatthaar, W. Hetaba, Y. Guo, J. Gallego, B. M. Smarsly and H. Over, *Chem. Mater.*, 2024, **36**(12), 6246–6256.

57 K. Kousi, D. I. Kondarides, X. E. Verykios and C. Papdopoulou, *Appl. Catal., A*, 2017, **542**, 201–211.

This journal is © The Royal Society of Chemistry 2025

J. Mater. Chem. A, 2025, **13**, 6451–6468 | **6467**

58 L. Falbo, C. G. Visconti, L. Lietti and J. Szanyi, *Appl. Catal., B*, 2019, **256**, 117791.

59 P. Panagiotopoulou, D. I. Kondarides and X. E. Verykios, *Appl. Catal., B*, 2009, **88**(3–4), 470–478.

60 K. Kousi, D. Neagu, L. Bekris, E. I. Papaioannou and I. S. Metcalfe, *Angew. Chem., Int. Ed.*, 2019, **59**(6), 2510–2519.

61 K. Kousi, D. Neagu, L. Bekris, a E. Calì, G. Kerherve, E. I. Papaioannou, D. J. Payne and I. S. Metcalfe, *J. Mater. Chem. A*, 2020, **8**(25), 12406–12417.

62 A. Martinez Martin, S. Saini, D. Neagu, W. Hu, I. S. Metcalfe and K. Kousi, *J. CO$_2$ Util.*, 2024, **83**, 103784.

63 L. Lindenthal, J. Popovic, R. Rameshan, J. Huber, F. Schrenk, T. Ruh, A. Nenning, S. Löffler, A. K. Opitz and C. Rameshan, *Appl. Catal., B*, 2021, **292**, 120183.

64 Y. Zhuang, R. Currie, K. B. McAuley and D. S. A. Simakov, *Appl. Catal., A*, 2019, **575**, 74–86.

65 M. F. Santos, A. E. Bresciani, N. L. Ferreira, G. S. Bassani and R. M. B. Alves, *J. Environ. Manage.*, 2023, **345**, 118822.

66 B. Liang, H. Duan, X. Su, X. Chen, Y. Huang, X. Chen, J. J. Delgado and T. Zhang, *Catal. Today*, 2017, **281**, 319–326.

67 C.-S. Chen, W.-H. Cheng and S.-S. Lin, *Appl. Catal., A*, 2004, **257**(1), 97–106.

68 J. Ye, Q. Ge and C.-J. Liu, *Chem. Eng. Sci.*, 2015, **135**, 193–201.

69 Y. Liu and D. Liu, *Int. J. Hydrogen Energy*, 1999, **24**(4), 351–354.

70 M. Tommasi, S. N. Degerli, G. Ramis and I. Rossetti, *Chem. Eng. Res. Des.*, 2024, **201**, 457–482.

71 J. H. Kwak, L. Kovarik and J. Szanyi, *ACS Catal.*, 2013, **3**(110), 2449–2455.

72 A. Aitbekova, L. Wu, C. J. Wrasman, A. Boubnov, A. S. Hoffman, E. D. Goodman, S. R. Bare and M. Cargnello, *J. Am. Chem. Soc.*, 2018, **140**(42), 13736–13745.

73 D. H. Kim, S. W. Han, H. S. Yoon and Y. D. Kim, *J. Ind. Eng. Chem.*, 2015, **23**, 67–71.

74 A. G. Kharaji, A. Shariati and M. A. Takassi, *Chin. J. Chem. Eng.*, 2013, **21**(9), 1007–1014.